PCCP

Accepted Manuscript

This article can be cited before page numbers have been issued, to do this please use: A. Cadranel, J. Tate, P. Oviedo, S. Yamazaki, J. H. Hodak, L. M. Baraldo and V. D. Kleiman, *Phys. Chem. Chem. Phys.*, 2016, DOI: 10.1039/C6CP06562G.

This is an Accepted Manuscript, which has been through the Royal Society of Chemistry peer review process and has been accepted for publication.

Accepted Manuscripts are published online shortly after acceptance, before technical editing, formatting and proof reading. Using this free service, authors can make their results available to the community, in citable form, before we publish the edited article. We will replace this Accepted Manuscript with the edited and formatted Advance Article as soon as it is available.

You can find more information about Accepted Manuscripts in the author guidelines.

Please note that technical editing may introduce minor changes to the text and/or graphics, which may alter content. The journal's standard Terms & Conditions and the ethical guidelines, outlined in our author and reviewer resource centre, still apply. In no event shall the Royal Society of Chemistry be held responsible for any errors or omissions in this Accepted Manuscript or any consequences arising from the use of any information it contains.

View Article Online
DOI: 10.1039/C6CP06562G

Journal Name

ARTICLE

Distant ultrafast energy-transfer in a trimetallic {Ru-Ru-Cr} complex facilitated by hole delocalization

Received 00th January 20xx,
Accepted 00th January 20xx

DOI: 10.1039/x0xx00000x

www.rsc.org/

Alejandro Cadranel[a†], Jaired Tate[b†], Paola S. Oviedo[a†], Shiori Yamazaki[b], José H. Hodak[a], Luis M. Baraldo*[a], and Valeria D. Kleiman*[b]

Multi metallic complexes based on {Ru-Cr}, {Ru-Ru} and {Ru-Ru-Cr} fragments are investigated for their light-harvesting and long-range energy transfer properties. We report the synthesis and characterization of $[Ru(tpy)(bpy)(\mu\text{-}CN)Ru(py)_4Cl]^{2+}$ and $[Ru(tpy)(bpy)(\mu\text{-}CN)Ru(py)_4(\mu\text{-}NC)Cr(CN)_5]$. The intercalation of$\{Ru^{II}(py)_4\}$ linked by cyanide bridges between the {Ru(tpy)(bpy)} and $\{Cr(CN)_5\}$ results in efficient, distant energy transfer followed by emission from the Cr moiety. Characterization of the energy transfer process based on photophysical and ultrafast time-resolved absorption suggests the delocalization of hole in the excited state, providing a pathway for energy transfer between the end moieties. The proposed mechanism opens the door to utilize this family of complexes as an appealing platform for the design of antenna compounds as the properties of the fragments could be tuned independently.

Introduction

Photoinduced intramolecular electronic energy transfer phenomena have been widely studied due to their key role in energy conversion systems.[1, 2,3-5] The design of molecular antennae[6-9] has been dominated by the vectorial model,[10-14] where energy migration occurs efficiently in a cascade fashion. This approach imposes some constrains to the palette of chromophores and the synthetic strategies implemented, because of the spatial arrangement of chromophores and the energy order requirement. A different approach to the construction of molecular antennae relays on the possibility of mixing the electronic wavefunctions of excited states of supramolecular components. For a donor-acceptor system, the introduction of an intermediate molecular component between donor and acceptor can lead to the electronic mixing among the donor and the new-moiety electronic states, which in turns leads to coupling to the acceptor. This excited state coupling can result in the opening of an effective direct path for the energy transfer process between donor and acceptor.[15, 16] If, in addition, the intermediate molecular component is a chromophore, it provides the beneficial effect of broadening the absorption spectrum and thus improving the light- harvesting properties of the antennae. Provided that the energy can be spatially directed to an acceptor, the design of broadband absorption multiple-chromophore antennae, multiple-component molecular antennae is a promising area to investigate.

Polynuclear transition metal complexes comprising ruthenium polypyridine units as building blocks are of great interest for constructing multicomponent systems (supramolecular systems) that are able to perform useful photoinduced functions[12] such as light harvesting,[17-20] and conversion of light into electrical[21-24] and chemical energy.[25, 26] An attractive feature of ruthenium polypyridine complexes is the ability to tune ground and excited state properties via a systematic variation of properties of the ligands.[27, 28]

[a] Departamento de Química Analítica, Inorgánica y Química Física, INQUIMAE, Facultad de Ciencias Exactas y Naturales, Universidad de Buenos Aires, Pabellón 2, Ciudad Universitaria, C1428EHA, Buenos Aires, Argentina. email: baraldo@qi.fcen.uba.ar
[b] Department of Chemistry, University of Florida. PO BOX 117200 Gainesville FL 32611-7200 USA. e-mail: kleiman@ufl.edu
† These authors contributed equally to the work.
Electronic Supplementary Information (ESI) available: DOI: 10.1039/x0xx00000x

View Article Online
DOI: 10.1039/C6CP06562G

The bipyridine ligand is used extensively in ruthenium based complexes such as $\{Ru(bpy)_2L_2\}$, but the use of bidentate ligands (such as bpy) in multicomponent systems gives rise to undesirable stereoisomers. Geometric isomers (*cis/trans*) exist in bis(bidentate) complexes, as well as enantiomers (Δ and Λ) for the *cis* form. Studies have shown that *cis* and *trans* isomers of a $\{Ru(bpy)_2L_2\}$ complex differ in energy by 40 kJ/mol.[29] In polynuclear systems based on bis(bidentate) centers, the possibility of stereoisomers increases exponentially as the number of metal centers increases.[30] Thus, the isomeric ambiguity conferred upon the system by use of bidentate ligands is a complicating factor in the design of polynuclear arrays. The bis-tridentate analogue, $[Ru(tpy)_2]^{2+}$, does not have stereoisomers, which allows for more control over linear polynuclear assemble, but possesses a relatively short excited state lifetime (125 ps)[31] compared to the ~900 ns lifetime for $[Ru(bpy)_3]^{2+}$. The short excited state lifetime of the MLCT state of bis-tridentate complexes like $[Ru(tpy)_2]^{2+}$ compared to bidentate analogues results from a distortion from octahedral geometry in the bis-tridentate configuration, which confers weaker field strength on the system.[32,33, 34,35] The weaker field strength makes thermal activation of a metal-centered (MC) state possible, followed by fast relaxation to the ground state.[36] Hence, to exploit the geometric advantages of using a *mer*-coordinating tridentate ligand and the extended lifetime afforded by use of a bidentate ligand, a heteroleptic chromophore with a bipyridine ligand and a terpyridine ligand seems to be a suitable candidate as a light absorbing unit in a polynuclear system.

While designing supramolecular systems with multiple metal centers it is crucial to choose the proper ligand to be used as metal-metal bridge. The cyanide bridge has been extensively used by coordination chemists to build molecular wires,[17, 18] antennae[21, 22, 37, 38] and other systems[39, 40] whose performance depends on the efficient mixing between the metal-centered electronic states. This bridge is able to promote strong coupling between metal ions, as exemplified by a trimetallic mixed-valence complex where the ground-state electron density is completely delocalized over the three ruthenium ions.[18] Hence this pseudohalide is an attractive alternative to construct supramolecular systems where a high extent of electronic communication is desired.

In previous work we have shown efficient energy transfer from a ruthenium polypyridine donor to an hexacyanochromate acceptor in the donor-acceptor {Ru-Cr} dyad $[Ru(tpy)(bpy)(\mu\text{-}NC)Cr(CN)_5]^-$ (**1**).[37] Emission from a chromium-centered dd (MC) state was detected upon visible light absorption by the {Ru(tpy)(bpy)} fragment. Here we report on a trimetallic system where we have intercalated a Ru moiety ($\{Ru^{II}(py)\}_4$) linked by cyanide bridges between the same donor and acceptor fragments. The resulting triad $[Ru(tpy)(bpy)(\mu\text{-}CN)Ru(py)_4(\mu\text{-}NC)Cr(CN)_5]$ (**3**) presents emission from the hexacyanochromate when irradiated in the UV and in the visible. We present the complete characterization of the energy transfer process based on photophysical and time-resolved data of these compounds. To better understand the properties of the excited states leading to energy transfer, we also investigate the properties of the bimetallic complex $[Ru(tpy)(bpy)(\mu\text{-}CN)Ru(py)_4Cl]^{2+}$ (**2**).

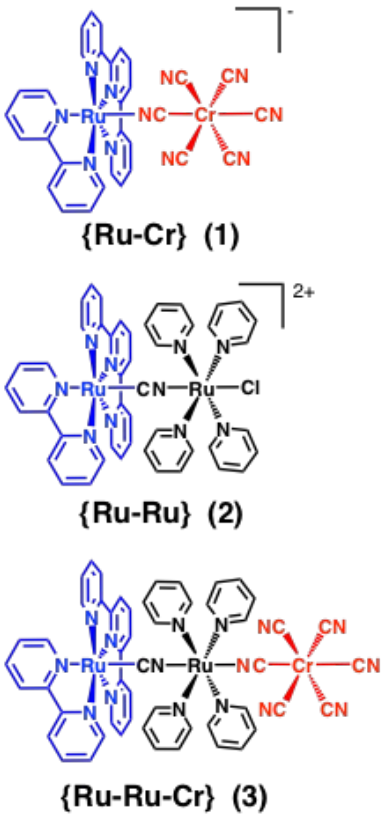

Scheme 1 Sketches for compounds **1**, **2**, and **3**.

Scheme 1 summarizes the compounds discussed in this report. The three systems include a {Ru(tpy)(bpy)} moiety (black). Bimetallic complex **1** and trimetallic complex **3** also include a $\{NC\text{-}Cr(CN)_5\}$ moiety whose ^{2}MC (metal centered) states can act as energy acceptors. Dyad **2** and triad **3** also include the $\{Ru(py)_4\}$ moiety, whose metal to ligand charge transfer (MLCT) state is energetically higher than the MLCT state of the {Ru(tpy)(bpy)}.

Materials and methods

$[Ru(py)_4Cl(NO)](PF_6)_2$,[41] $[Ru(tpy)(bpy)CN](PF_6)$,[37] $(TPP)_3[Cr(CN)_6]$[42] and **1**[37] were prepared according to published procedures. Solvents for electrochemical, spectral and spectroelectrochemical measurements were dried using a PureSolv Micro solvent purification system. All other reagents were obtained commercially and used as supplied. The compounds synthesized were dried in a vacuum desiccator for at least 12 hours prior to characterization.

Synthetic Procedures. $[Ru(tpy)(bpy)(\mu\text{-}CN)Ru(py)_4Cl](PF_6)_2$ ([2](PF$_6$)$_2$). 200 mg of $[Ru(py)_4Cl(NO)](PF_6)_2$ (0.26 mmol) were dissolved in 10 mL of argon-saturated acetone, and 17.8 mg (0.26 mmol) of NaN_3 were added. After 40 minutes under argon atmosphere, there was no more unreacted NaN_3 and the solution turned to an amber color. 150 mg of

View Article Online
DOI: 10.1039/C6CP06562G

[Ru(tpy)(bpy)CN](PF$_6$) (0.22 mmol) were added and the mixture was stirred in darkness under argon atmosphere at room temperature for 9 days. Then, 10 mL of a saturated aqueous solution of KPF$_6$ were added, the solution was evaporated to 10 mL and a dark solid appeared. It was filtered and redissolved in a minimum volume of a 1:1 acetone/methanol mixture. After filtering a yellow solid, the liquors were loaded on a Sephadex LH-20 column (l = 60 cm, **φ** = 4 cm) packed in 1:1 acetone/methanol. Elution was performed gradually increasing the methanol proportion. The first (orange) and third (yellow) collected fractions were disposed, while the second one (violet) was evaporated until 5 mL remained. 5 mL of a saturated aqueous solution of KPF$_6$ were added, and a dark solid was filtered and washed with water at room temperature (2 x 3 mL). Yield: 122 mg (42 %). Anal. Calc. for **[2](PF$_6$)$_2$·1.5H$_2$O**: C, 43.0; H, 3.3; N, 10.9. Found: C, 43.2; H, 3.3; N, 10.6. ^{1}H NMR (500 MHz, acetone-d_6): δ (ppm) 9.87 (dd, 1H, Ha), 8.88 (d, 1H, Hd), 8.83 (d, 2H, H5), 8.68 (d, 1H, He), 8.67 (d, 2H, H4), 8.43 (t, 1H, H6), 8.36 (ddd, 1H, Hc), 8.13 (ddd, 2H, H3), 8.08 (dd, 8H, Hα), 8.02 (ddd, 2H, H1), 8.01 (m, 1H, Hf), 7.92 (ddd, 1H, Hb), 7.76 (tt, 4H, Hγ), 7.63 (d, 1H, Hh), 7.50 (ddd, 2H, H2), 7.30 (ddd, 1H, Hg), 7.10 (dd, 8H, Hβ). Proton labeling is detailed in Figure **S1**.

[Ru(tpy)(bpy)(μ-CN)Ru(py)4(μ-NC)Cr(CN)$_5$] (**3**). 150 mg of **[2](PF$_6$)$_2$** (0,12 mmol) were dissolved in 50 mL of acetone, and 730 mg of (TPP)$_3$[Cr(CN)$_6$] (5 equivalents) were dissolved in 100 mL of methanol. Both solutions were mixed, and 10 mL of water were added. The dark red mixture was refluxed for 4 hours, and an orange material precipitated. After filtering and washing with acetone (2 x 3 mL) and methanol (2 x 3 mL) at room temperature, the solid was dissolved in 1:1 DMSO/H$_2$O. Slow diffusion of acetone resulted in a microcrystalline red solid, which was filtered and washed with water (2 x 3 mL) at room temperature. Yield: 32 mg (22 %). Anal. Calcd.: **[3]·6H$_2$O·DMSO**: C, 48.8; H, 4.3; N, 16.9; S, 2.4. Found: C, 48.9; H, 4.2; N, 16.7; S, 2.1.

Steady state characterization. Crystal structure of compounds **2** and **3** were determined with an Oxford Xcalibur, Eos, Gemini CCD area-detector diffractometer using graphite-monochromatic Mo-*K*α radiation (*λ* = 0.71069 Å) at 298 K. Data was corrected for absorption with CrysAlisPro, Oxford Diffraction Ltd., Version 1.171.33.66, applying an empirical absorption correction using spherical harmonics, implemented in SCALE3 ABSPACK scaling algorithm.[43] The structures were solved by direct methods with SIR 97[44] (compound **2**) SHELXS-97[45] (compound **3**) and refined by full-matrix least-squares on F^2 with SHELXL-2014[46] under WinGX platform.[47] Hydrogen atoms were added geometrically and refined as riding atoms with a uniform value of U_{iso}, with the exception of hydrogen atoms of the water solvent molecules in the case of **3**. These were not located in the difference map and hence were not included in the model. One of these water molecules (O7W) was refined disordered over two positions with 0.5:0.5 occupation numbers.

IR spectra were collected with a Nicolet FTIR 510P instrument, as KBr pellets. UV–visible spectra were recorded with a Hewlett-Packard 8453 diode array spectrometer (range 190–1100 nm). ^{1}H-NMR spectra were measured with a Bruker ARX500 spectrometer, using deuterated solvents from Aldrich. Elemental analyses were carried on a Carlo Erba 1108 analyzer with an estimated error of ± 0.5%. Electrochemical measurements were performed under argon with millimolar solutions of the compounds, using a TEQ V3 potentiostat and a standard three electrode arrangement consisting of a glassy carbon disc (area = 9.4 mm^2) as the working electrode, a platinum wire as the counter electrode and a silver wire as reference electrode plus an internal ferrocene (Fc) standard. Tetra-*n*-butylammonium hexafluorophosphate ([TBA]PF$_6$, 0.1 M) was used as the supporting electrolyte. All the potentials reported in this work are referenced to the standard Ag/AgCl saturated KCl electrode (0.197 V vs. NHE), the conversions being performed with literature values for the Fc$^+$/Fc couple.[48] Excitation and emission spectra were recorded in the near IR in a PTI-QuantaMaster 50. Quantum yields were measured in Argon-saturated solutions (λ_{exc}=460 nm) using [Ru(bpy)$_3$]$^{2+}$ (ϕ = 0.095[28] in ACN at 25 °C) as reference.

Time resolved experiments. Time resolved luminescence measurements for **2** were made using a PicoQuant time harp 200 card, with a home built pulsed laser centered at 450 nm (instrument response 1 ns FWHM) as the excitation source. Emission was filtered by a 520 nm cut-off filter. In the case of compounds **1** and **3**, excitation was done with the output of a femtosecond optical parametric amplifier at 532 nm (<200 fs FWHM pulses). The emission was collected with a 5 cm focal length lens and focused on the entrance of a monochromator (Oriel 77250). The signal was detected with a photomultiplier tube (Hammamatsu R928) and a 500 MHZ digitizing oscilloscope (Agilent MSO5062A).

Transient absorption experiments were done using a broadband home-built apparatus. A commercial 1 kHz Ti:Sapphire regenerative amplifier laser system (SpectraPhysics) produces 800 mW of 65 fs pulses centered ~800 nm. Roughly half (400 mW) of the output of this amplifier is used for transient absorption experiments. A 99:1 beamsplitter divides the beam with 1% used to generate a white light continuum for the probe beam, while the rest is used to seed an optical parametric amplifier (OPA) providing excitation wavelength tunability. The experiments described herein used either 490 nm excitation, generated by sum-frequency generation of the amplifier output and the OPA signal beam, or 400 nm generated by second-harmonic generation of the regenerative amplifier output. The white light continuum was generated by focusing the 800 nm beam onto a CaF$_2$ plate, and further divided into probe and reference beams. The pump beam traveled through a retroreflector mounted on a motorized translation stage to vary the delay time, through an optical chopper to generate "pump ON" and "pump OFF" cycles, and spatially overlapped with the probe beam at the sample position. The beam sizes of pump and probe beams were measured to be ~260-275 μm and <100 μm, respectively. Probe and reference beams were focused onto a spectrograph and detected using a CCD camera. The relative polarization between the pump and

View Article Online
DOI: 10.1039/C6CP06562G

probe beams was set to magic angle (54.7°) to avoid rotational decay artifacts. All samples for transient absorption experiments were held in a 2-mm quartz cuvette, capped with a rubber septum and degassed under argon for 20-30 minutes. The optical density of each sample was kept between 0.3 and 0.5 at the excitation wavelength. Photodegradation of the samples was monitored by taking the absorption spectrum of each sample before and after the transient absorption experiments. Each broadband spectrum represents the averaging of ~45K laser shots.

Data collection for the transient absorption experiments results in a two-dimensional array. Each row consists of a full spectrum recorded at a specific delay time (time-gated spectrum), and each column corresponds to the absorption change at a particular wavelength over time (kinetic trace). The kinetic traces were fit using an exponential function convoluted with a Gaussian to represent the instrument response function (which was measured using the Raman response of the solvent) represented by

$$\Delta A(\lambda) = c_0 + \sum_{i=1}^{n} \frac{c_i}{2\tau_i} \exp\left(\frac{\sigma^2}{2\tau_i^2} - \frac{t-t_0}{\tau_i}\right)\left[1 - \mathrm{erf}\left(\frac{\sigma}{\sqrt{2}\tau_i} - \frac{t-t_0}{\sqrt{2}\sigma}\right)\right]$$

where $\sigma = \mathrm{FWHM}_{Gaussian}/2\sqrt{\ln 2}$, t_0 represents time zero, τ_i represents the i^{th} time constant, c_0 represents a vertical offset, and c_i represents an amplitude factor for the i^{th} component.

Results and Discussion

Synthesis.

The synthesis of the complexes reported here are based on the reaction of azide with the nitrosyl moiety on the complex $[Ru(py)_4Cl(NO)]$ that results in a labile solvent-complex.[41, 49] In the case of **2**, reflux temperatures are avoided to prevent the formation of oligomeric complexes through chloride labilization. Thus, it is necessary to perform the reaction several days for the positive nitrile (i.e. $[Ru(tpy)(bpy)(CN)]^+$) to substitute a solvent molecule at the also positive $[Ru(py)_4Cl(sv)]^+$ center. The preparation of **3** takes full advantage of the possibility of asymmetrically di-substituting the $\{Ru(py)_4\}$ moiety. It involves the replacement of the chloride ligand in **2** at reflux temperatures. Purification is a major concern in the case of **3**. Its neutral state of charge precludes counter-ion exchanges and regular precipitation techniques, and its poor solubility properties in a wide variety of solvents prevent the use of chromatographic methods.

Characterization

Crystal Structure. Slow evaporation of a solution of **2** in acetone, and slow diffusion of acetone in a solution of **3** in DMSO, yielded single crystals suitable to determine the X-ray crystallographic structures of **2** and **3**. Table **S1** collects selected bond distances and angles, while additional crystallographic data and values of R_1 and *w*R are listed in Table **S2**;[50] Figure **1** shows their structures. Compounds **1**[37] and **3** show one of the cyanides N-bound to the Ru moiety, while the bridge between the two ruthenium units in **3** shows the N facing the $\{Ru(py)_4\}$ side.[42]

The {Ru(tpy)(bpy)} fragment displays a distorted octahedral geometry around the metal ion (Ru_{tpy}) in **2** and **3** as found in **1**[37] and other structural similar complexes,[51,52, 53,54-56] Short Ru-N distances to the central ring of the terpyridine, and N-Ru-N angles < 80° are imposed by the rigid structure of the polypyridyl ligands. For **2** and **3**, The $\{Ru(py)_4\}$ moiety presents in both cases a propeller-like configuration and Ru-N_{py} distances ranging 2.076-2.112 Å, similar to what is observed in previously reported analogues.[38, 57]

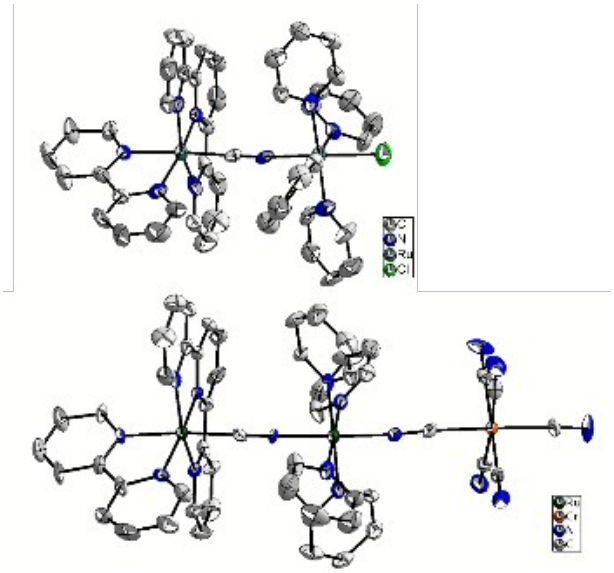

Figure 1 Crystal structure of complexes **2** and **3**. Ellipsoids are drawn with 30% displacement probability. Hydrogen atoms and solvent molecules were omitted for clarity.

The C-N distance of the cyanide bridging Ru_{tpy} with Ru_{py} is longer for **2** than for **3**. Chloride is known to have better donor abilities than nitriles,[57] which results in an electron-richer $\{Ru(py)_4\}$ center. The π back-bonding from this moiety to N-bonded cyanide bridge brings more electronic density on the bridge π* orbitals in **2**, enlarging that C-N bond. In **3**, a similar effect is observed for the Cr-bound cyanide bridge, whose C-N distance is unusually long (1.177 Å against 1.144-1.149 Å in other $\{Ru^{II}(\mu\text{-}NC)M^{III}(CN)_5\}$ analogues.[37, 38] The observed angles along the Ru_{tpy}-Ru_{py} axis are close to 180° for **2** and **3**, but those angles along intermetallic axis involving the $\{Cr(CN)_6\}$ fragment in **1** and **3** deviate from linearity (from 167.8° to 174.8°). This deviation from linearity has already been observed in related compounds,[38] and has been attributed to specific interactions in the solid state involving the exposed cyanide ligands. In **3**, four of the five exposed cyanides are involved in hydrogen bonding interactions with solvation water molecules in the crystal. Hence, the trimetallic complex **3** is likely to display an almost linear configuration in solution, which favors metal-metal communication and orbital overlap along the intermetallic axis.

View Article Online
DOI: 10.1039/C6CP06562G

Electrochemistry

As reported previously,[37] the cyclic voltammogram of the bimetallic complex **1** in acetonitrile shows one reversible anodic process (Figure **2**, top panel) associated with the oxidation of the ruthenium moiety, followed by two reversible

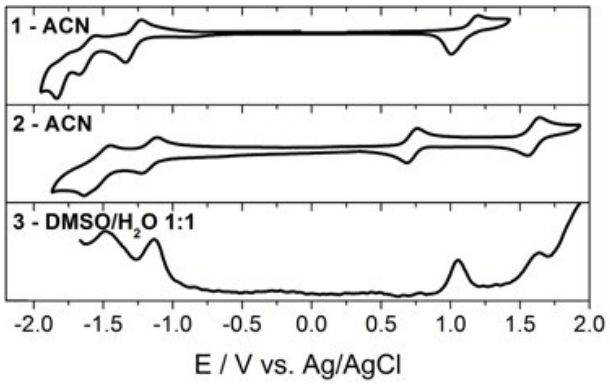

Figure 2 Electrochemistry of complexes **1** - **3**. Cyclic voltamograms for **1** and **2** were collected in acetonitrile with a scan rate of 100 mV/s. For compound **3** the solvent is DMSO/H_2O 1:1 and square wave voltammetry was used instead of cyclic voltammetry due to the low solubility of the complex.

reductions of the ligands and a reduction process which is irreversible due to loss of ligand on the generated Cr(II). For the bimetallic complex **2** (middle panel), two anodic process are observed corresponding to the oxidation of the two ruthenium centers. We assign the one at lower potential to the oxidation of the ruthenium in the {$Ru(py)_4Cl$} fragment, displaced cathodically by the presence of the chloride ligand, while the process at 1.6 V corresponds to the oxidation of the metal center in the {Ru(tpy)(bpy)} moiety. Square wave voltammetry measurements of **3** in a DMSO/H_2O mixture (bottom panel) reveals two reversible anodic waves assigned to oxidation of the ruthenium ions (Table **S3**). Here, we also attribute the process at lower potential to the {$Ru(py)_4$} moiety, while the wave at 1.64 V corresponds to the oxidation of the {Ru(tpy)(bpy)} fragment.

Photophysical Properties

Infrared. IR absorption spectra of the three compounds (Figure **3**) were measured in the 2000-2200 cm^{-1} region to identify CN stretching bond frequencies (assignment listed in Table **S4**) under different environments. All compounds show bands near 2100 cm^{-1}, where typical hexacianometallates(III) absorb. Bimetallic complex **1** shows split CN stretching bands with the strongest contribution at 2119 cm^{-1} assigned to the terminal groups, while the weak band at lower frequencies is likely due to the bridge ligand.[37, 38] In the compounds containing two ruthenium ions, the bridge cyanide group appears at 2096 cm^{-1} (in **2**) and 2104 cm^{-1} (in **3**). The shift to lower frequencies for **2** is consistent with the weakening of the C-N bond due to the back-bonding from the {$Ru(py)_4Cl$} which results in increased population of the cyanide π* orbitals. Triad **3** shows additional peaks at 2127 cm^{-1} and 2120 cm^{-1} assigned as the chromium-bound cyanides, by comparison with **1** and other complexes containing the hexacyanochromate(III) moiety.[58, 59]

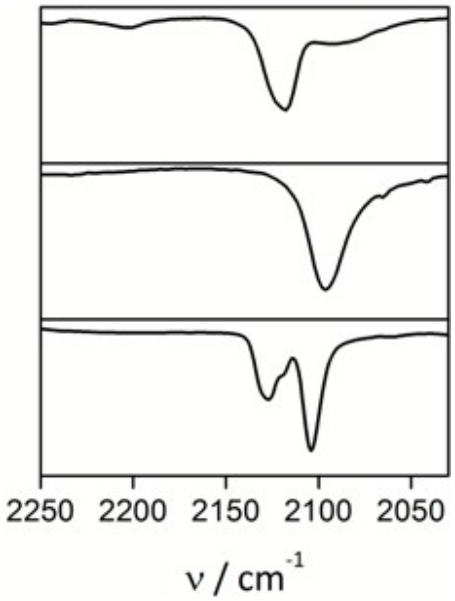

Figure 3: IR absorption spectra in the CN^- stretching region of **1**, **2** and **3** (top to bottom) in KBr pellets. Assignment information can be found in Table **S4**

UV-Vis. The UV-Vis absorption spectra of the three complexes (Figure **4,** black curves, with assignments listed in Table **S5**) show similar features. Complexes **2** and **3** also present intense absorption bands at 380 nm (**2**) and 363 nm (**3**) corresponding to MLCT π*(py)←dπ(Ru) transitions. The lower energy bands, appearing as a shoulder ~440 nm for **2** and at ~460 nm for **3**, correspond to MLCT transitions involving acceptor orbitals on the tpy (π*(tpy)←dπ(Ru)) and bpy (π*(bpy)←dπ(Ru)) ligands. For dyad **1**, the (π*(tpy)←dπ(Ru)) transition is centered at 478 nm with some likely contribution from the bpy ligand appearing as a shoulder at ~ 423 nm. Low intensity broad MM'CT Cr(III) ←Ru(II) transitions are also expected for **1** and **3**, but are probably overlapped with the MLCT bands.

All the complexes reported here present room temperature photoluminescence; their excitation (red) and emission (blue) profiles are illustrated in Figure **4** and the key parameters are collected in Table **3**. Complex **1** presents a typical chromium-centered NIR emission centered at 811 nm with a 49 μs lifetime in DMSO (Figure **S2**), sensitized by the {Ru(tpy)(bpy)} chromophore. The excitation spectrum follows closely its absorption spectrum in the visible spectral range, which corresponds to {Ru(tpy)(bpy)} MLCT excitation with weak activity in the blue end. A very weak emission at ~700 nm can also be distinguished which coincides with the maximum emission of the $[Ru(tpy)(bpy)CN]^{2+}$ monomer.[37] Dyad **2** shows a weak and broad emission at 690 nm in DMSO with a lifetime of 5.6 ns (Figure **S2**). The excitation spectrum of **2** presents a band peaked at 493 nm with some additional weak activity in

View Article Online
DOI: 10.1039/C6CP06562G

the blue side of the spectrum. The energy and lifetime of this emission are similar to those reported for monometallic and bimetallic complexes presenting the same {Ru(tpy)(bpy)} fragment and suggest that this emission results from a ^{3}MLCT state. [60, 61]

The trimetallic complex **3** shows a small emission band near 700 nm and a strong and narrow NIR emission at 840 nm. The energy of the latter together with its bandwidth and lifetime (15 µs, Figure **S2**) allow us to assign its origin as a chromium ^{2}MC state.[37] As observed for the {Ru-Ru} dyad **2**, the excitation spectrum of the {Ru-Ru-Cr} triad **3** tracks the red side of the absorption spectrum (Figure **4**, bottom panel). Taken together, the evidence indicates that in compound **3** there is efficient energy transfer from the {Ru(tpy)(bpy)} fragment to the hexacyanochromate ion; even in the presence of the {Ru(py)$_4$} unit between sensitizer and sensitized chromophores. This process is similar to the efficient energy transfer previously observed for the {Ru-Cr} dyad **1.** [37]

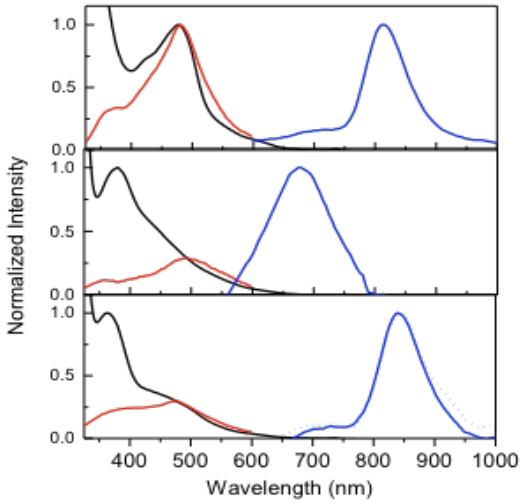

Figure 4: Absorption (——), excitation (——), and emission (——) spectra for **1** (top), **2** (middle), and **3** (bottom) in DMSO. The emission spectra were taken after excitation in the π*(tpy) ←t_{2g}(Ru) MLCT region. Excitation spectra were collected at the wavelength of emission maximum. Absorption and excitation data are normalized at the wavelength of the MLCT band maximum, while emission data are normalized at the peak wavelength.

Comp.	Emission				
	λ_{em} / nm (ϕ_{em} x 10^3)		τ / µs	τ_{EnT} (ps)	η_{EnT}
	MLCT(Ru)	MC(Cr)			
1[37]	684 (0.01)	817 (3.3)	49	4.1	0.99*
2	677 (0.6)	-	5.6x10^{-3}		-
3	673 (0.06)	835 (0.90 Ru_{tpy}) (0.23 Ru_{bpy})	15	170	0.97
$[Cr(CN)_6]^{3-}$	-	805 (0.7)	90		

Table 1: Photophysical information for the three multi-metal systems in DMSO. Emission lifetime of donor **1** was measured in ACN. It is expected to be slightly shortened in DMSO, not enough not impact the energy transfer efficiency calculation.

Excited states Photophysics

Broadband differential transient absorption. In order to understand the dynamics in the excited state and to characterize the energy transfer process we explore the early time dynamics following excitation at selective wavelengths. Broadband transient absorption spectra were collected following excitation at 490 nm (Figure **5**) which corresponds to initial excitation of the π*←t_{2g} MLCT transition centered in the {Ru(tpy)(bpy)} moiety and, in a separate experiment, following excitation at 400 nm (Figure **S3**) where the initial excitation reaches the π*←t_{2g} MLCT transition centered in the {Ru(py)$_4$} moiety.

Spectral Profiles. Figure **5** shows differential absorption spectra of the three compounds in DMSO upon 490 nm excitation. The wavelength axis has been expanded in the high-energy region where the most critical transitions can be observed. The top panel corresponds to the {Ru-Cr} dimer **1**. Its early time spectra show three distinctive features: a positive absorption associated with ligand centered (LC) excited state absorption, centered at 384 nm; a negative absorption associated with removal of ground state population ~470 nm; and a positive absorption at wavelengths longer than ~550 nm. This is consistent with the characteristic electronic absorption of MLCT states of ruthenium polypyridine complexes. Assignment of these bands is based on similar measurements on related complexes [62-67]and on the results from spectro-electrochemistry. The positive band observed in the 350-400 nm region is assigned to LC transitions of the reduced terpyridine present in the MLCT state. The negative absorption corresponds to the absence of the π*←t_{2g}(Ru) transition as the MLCT excited state has a Ru^{III}(bpy)(tpy)$^{\delta-}$ character, while the positive absorption band above 500 nm corresponds to a Ru(III)←π LMCT transition with a small contribution from π*←π* transitions centered in the reduced ligand.[66, 68]

The middle panel shows the broadband transient spectra of

View Article Online
DOI: 10.1039/C6CP06562G

the {Ru-Ru} dimer **2**. There is a negative absorption at the energy where the excited π*(tpy) ←t_{2g}(Ru) transition is assigned. Additionally, a transient negative absorption band at 380 nm is observed. From the steady state absorption spectrum we assign this signal to the absence of the π*(py) ←t_{2g}(Ru) MLCT absorption observed in the ground state. In the UV region, peaked at 350 nm, the excited state absorption (ESA) follows the same assignment as in **1**. This positive absorption band appears blue-shifted because the negative signal (due to the π*(py) ←t_{2g}(Ru) transition) overlaps with the red edge of the positive excited state absorption. The simultaneous presence of the MLCT bleaches arising from both {Ru(tpy)(bpy)} and {Ru(py)$_4$} moieties upon excitation on the first fragment could be indicative of both Ru ions having some degree of Ru(III) character in the MLCT manifold.

Finally, the lower panel shows the differential spectra of the {Ru-Ru-Cr} triad **3** where we can identify the same transitions observed for **2**: ESA arising from LC transitions (347 nm), negative absorptions from the π*(py) ←t_{2g}(Ru) (390 nm) and π*(tpy) ←t_{2g}(Ru) (450 nm) MLCT transitions, and ESA at wavelengths longer than 600 nm.

The dynamics associated with the excited states of each compound will be analyzed independently.

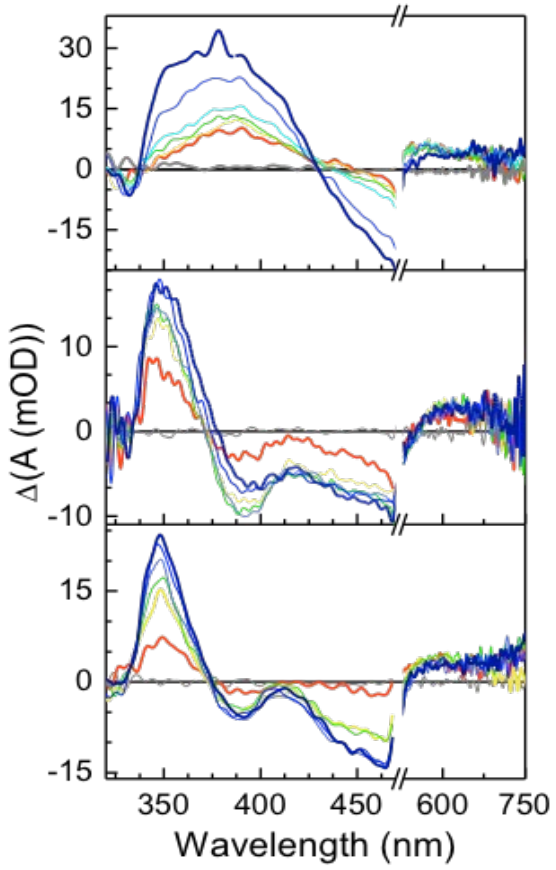

Figure 5: Broadband Transient absorption spectra of compounds **1**, **2**, and **3** in DMSO following excitation at 490 nm. The spectra shown correspond to negative times, 0.7 (—), 2.5 (—), 8 (—), 20 (—), 100 (—), 700 (—) ps. The gap in the *x*-axis (472-528 nm) is to remove pump scatter.

Early dynamics on the excited state

{Ru-Cr} dimer. In the case of dimer **1** (Figure **6**), within the first 10 ps we observe a decrease in the ESA (370 nm) accompanied by broadening, a decrease and narrowing of the negative absorption (470 nm) band while the ESA at longer wavelengths (λ > 500 nm) shows a slight increase in intensity (Figure **6**). These spectral changes indicate the formation of a new electronic state. By Δt = *20 ps*, the intensity of the signals has reached their long time values and remain constant for the duration of the observation window (800 ps), consistent with the measured emission lifetime of the complex, 49 μsec in DMSO. This final difference spectrum is due to the presence of the long-lived excited state responsible for the NIR emission, a bimetallic complex containing the Cr ion in a ^2E_g state. The low energy region (λ > 540 nm) of the transient final spectrum shown in Figure **5** is very congested; with overlapping of multiple photoinduced absorption bands associated with LMCT and Cr*←Ru MM*CT bands.[21] Kinetic traces for the three bands (354 nm, 460 nm, and 535 nm) are shown in Figure **6** and were globally fitted using the convolution of the instrument response function with exponential decays (all relevant fit parameters are listed in Table **4**). A τ = (4.1 ± 0.9) ps was obtained which corresponds to the energy transfer process from theexcited state to the Cr ^{2}MC -metal centered-state.[69]

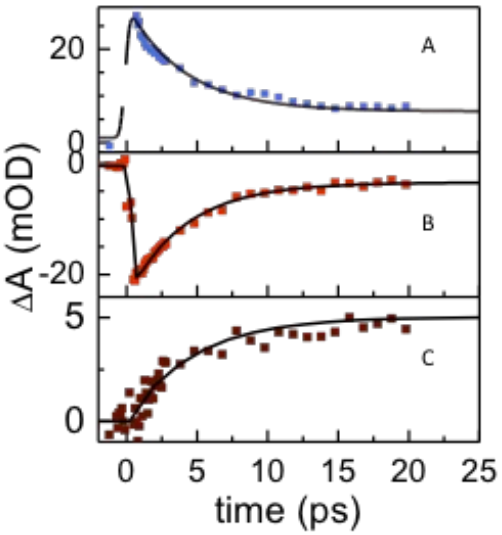

Figure 6: Kinetic traces for **1** following excitation at 490 nm. A) photoinduced absorption (~365 nm) B) negative absorption from π*(tpy) ←t_2g (Ru) (465 nm) and C) Photoinduced absorption from a Cr MC state (530 nm) .

View Article Online
DOI: 10.1039/C6CP06562G

Comp.	Assignment	λ_{obs} /nm	λ_{exc} = 490 nm		λ_{exc} = 400 nm	
			τ_1 (ps)	τ_2 (ns)	τ_1 (ps)	τ_2 (ns)
1	π*(tpy) ←t_{2g}(Ru)	460	4.1± 0.9	≳ 1		
	π*(tpy) ← π(tpy)	365				
	d(Cr) ← *d*(Cr)	530				
2	π*(py) ←t_{2g}(Ru)	360	1.7 ± 0.4	≳ 1	17 ± 2.3	
	π*(tpy) ←t_{2g}(Ru)	460				≳ 1
3	π*(py) ←t_{2g}(Ru)	360	1.8 ± 0.7	0.17 ± 0.05	16 ± 1.3	0.170 ± 0.004
	π*(tpy) ←t_{2g}(Ru)	460				0.170 ± 0.004

Table 2: Time constants obtained from global fit of kinetic traces

{Ru-Ru} dimer. To understand the processes occurring in **2**, we can use selective excitation of the π*←t_{2g} MLCT transition centered in the {Ru(tpy)(bpy)} moiety (λ_{exc} = 490 nm, Figure **5** middle panel) or the π*←t_{2g} MLCT transition centered in the {Ru(py)$_4$} fragment (λ_{exc} = 400 nm, Figure **S3**, top panel).

Upon excitation with λ_{exc} = 490 nm we observe the presence of two negative absorption bands of similar magnitude. In general, excitation of a transition results in a negative signal in the corresponding spectral region, but in this system we also observe a negative band associated with an MLCT transition that is not being excited (390 nm). At 490 nm excitation, the bleach of the π*(tpy) ←t_{2g}(Ru) MLCT at 460 nm is initially dominant, especially considering its smaller molar absorptivity compared with the other MLCT transition (Figure **4**). The evolution of the kinetic traces (Figure **7**, panel A) is also very informative. Rather than decaying or increasing together (which would indicate a common ground state), the behavior of the two negative absorption bands (390 nm and 460 nm) is complementary. Within the first 10 ps the negative absorption at high energy become more negative, while the one at low energy goes in the opposite direction. The ESA at 350 nm increases in the same time-scale. This points to a process where {Ru(py)$_4$} gains Ru(III) character at expenses of {Ru(tpy)(bpy)}. Global fit of these traces yields a ~1.7 ps for the common fast process with an additional time component longer than 1 ns. This long decay is consistent with the emission lifetime (5.6 ns) and suggests that the long term spectral profile corresponds to the difference spectra of the MLCT emitting state (Figure **5**).

Complex **2** was also excited at 400 nm, where the main contribution to absorption in the ground state is from the π*(py) ←t_{2g}(Ru) MLCT transition. The broadband differential spectra at different delays is shown in Figure **S3,** while the kinetic traces are shown in panel B of Figure **7**. The assignment of the transient bands is similar to that of Figure **5** (middle panel) although different dynamics are observed. In contrast with excitation at 490 nm, the magnitude of the negative absorption at 390 nm (~15 mOD) is larger than at 470 nm (~8 mOD), consistent with the transition that is being excited. This initially populated excited state presents a spectral profile remarkably similar to that predicted by oxidative spectroelectrochemistry (Figure **S4**), where the {Ru(py)$_4$} center is oxidized. Hence we conclude that upon 400 nm excitation the initially populated state has a substantial Ru(III) character on the {Ru(py)$_4$} fragment.

Following excitation, there is a decay in the negative absorption of the π*(py) ←t_{2g}(Ru) MLCT (green curve), while the intensity of the π*(tpy) ←t_{2g}(Ru) MLCT transition grows (the negative band becomes more pronounced). Both processes follow an exponential behavior with τ = 17 ps. This points to a process where {Ru(tpy)(bpy)} gains Ru(III) character at expenses of {Ru(py)$_4$}. After that, a longer (>1 ns) component leads to the population returning back to the ground state. This long lifetime is consistent with that observed at 490 nm excitation and indicates the differential spectrum from population of the same emitting state.

To understand the source of these dynamics at the two negative absorptions one should consider the nature of the excited state. Delocalization of the wavefunction has been observed in cyanide-bridged mixed valence complexes when the energies of the dπ orbitals are similar; Baraldo and coworkers have investigated a similar dinuclear complex, $[Ru^{II}(tpy)(bpy)\text{-}NC\text{-}Ru^{III}(py)_4CN]^{3+}$and reported time-dependent Density Functional Theory and spectroscopic results indicating that the electron density is delocalized between the two moieties despite the intrinsic asymmetry of the bridge.[18]

We propose that the excited state involved in the observed dynamics present different degrees of delocalization, resulting in the presence of both MLCT transitions in their spectra but with different intensities, and hence present the observed behavior at the selected wavelengths. After absorption at 400 nm, the initially excited state is a mixed valence complex with the hole centered mainly on the {Ru(py)$_4$} center. This is observed as a strong negative band at 390 nm with a less intense negative feature at 470 nm. As time evolves, the hole becomes more delocalized between the two metal centers with the correspondent decrease in the differential absorbance at 470 and an increase at 390 nm (Figure **7B**). This delocalization process takes about 17 ps.

View Article Online
DOI: 10.1039/C6CP06562G

Following excitation at 490 nm, a similar process occurs, although the initial mixed valence excited state is better described as a complex with the hole mainly localized in the {Ru (tpy)(bpy)} center. The decrease in negative intensity at 460 nm is consistent with the formation of a species with more Ru(II) character at this center than the initially photoinduced state created; likewise, for the 390 nm band, an increase in the magnitude of the negative absorption is indicative of diminishing character Ru(II) of the $\{Ru(py)_4\}$ metal center. The concerted dynamics of the transient absorption bands reflect the delocalization of the hole between the two Ru centers occurring in a 1.7 ps timescale.

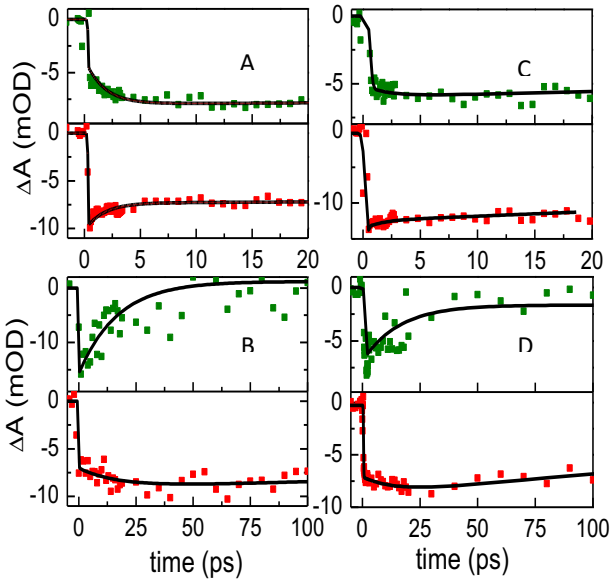

Figure 7: Early-times kinetic traces of **2** (left) and **3** (right), upon excitation at 490 nm (top) and 400 nm (bottom). The negative band detected at 350-365 nm (π^*(py) $\leftarrow t_{2g}$ (Ru)) is shown in green while the band corresponding to π^*(tpy) $\leftarrow t_{2g}$ (Ru) (450-465 nm) is shown in red.

{Ru-Ru-Cr} trimer. With insight gained on the excited state behavior of **1** and **2**, we explore the dynamics of **3** upon selective excitation of the {Ru(tpy)(bpy)} (Figure **5**, bottom panel) or $\{Ru(py)_4\}$ centered (Figure S**3**, bottom panel) MLCT transitions. The observed behavior upon excitation at 490 nm is reminiscent of the observed changes for **2**. The broadband spectra show a decay of the π^*(tpy) $\leftarrow t_{2g}$(Ru) negative signal while the π^*(py) $\leftarrow t_{2g}$(Ru) negative signal increases. Following this fast process, we observe a much slower decay of all the signals in the hundreds ps time scale. Global fit of the kinetic traces (Figure **7** panel C**)** reveals a time constant of 1.8 ps. This early dynamic component is similar to the behavior exhibited by **2**, with decrease in the intensity of the band associated with the π^*(tpy) $\leftarrow t_{2g}$(Ru) MLCT transition that was excited, and its time constant is nearly identical to the fast process exhibited by **2** upon 490 nm excitation. Transient absorption spectroscopy of **3** was also performed using 400 nm as the excitation wavelength, with the corresponding kinetic traces shown in Figure **7,** panel **D**. The early time response mimics the results obtained for **2**, with a 16 ps time constant for the decay of the π^*(py) $\leftarrow t_{2g}$(Ru) and concomitant increase of the π^*(tpy) $\leftarrow t_{2g}$(Ru) band. Accordingly, the fast dynamics exhibited by complex **3** is assigned to a transition between two

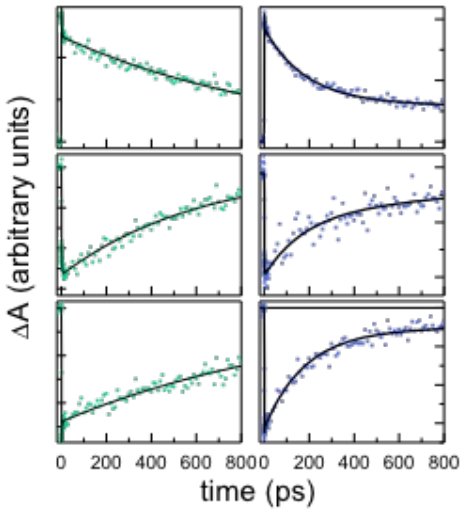

Figure 8: Long-time kinetic traces for **2** (left) and **3** (right) following excitation at 490 nm. Top panel: photoinduced absorption (~350 nm) Middle panel: negative absorption from π^*(py) $\leftarrow t_{2g}$ (Ru) (390 nm) and Bottom panel: Negative absorption from π^*(tpy) $\leftarrow t_{2g}$ (Ru) (450-460 nm) .

excited states with different degrees of delocalization similar to the fast process assigned for **2**. The state populated at 400 nm seems to have an additional path of deactivation that leads to a slightly smaller emission quantum yield observed upon excitation of the π^*(py) $\leftarrow t_{2g}$(Ru) band (Table **3**) as well as the lower intensity of the π^*(py) $\leftarrow t_{2g}$(Ru) band in the excitation spectrum (Figure **4**).

Late dynamics on the excited state.

Comparison of the long time kinetic traces of **2** and **3** are shown in Figure **8** for three different detection bands following excitation at 490 nm. In **3**, the presence of the $\{Cr(CN)_6\}$ acceptor introduces a new pathway for MLCT deactivation. The time constant associated with this process is 170 ps. The appearance of this decay -not observed in **2** where no Cr acceptor is present- together with the steady state spectroscopy showing emission from the Cr center through {Ru(tpy)(bpy)} sensitization (Figure **4**, bottom panel) allow us to assign this new path to energy transfer from the low lying MLCT to the Cr unit. A similar decay is observed upon 400 nm excitation and is also assigned to energy transfer to the $\{Cr(CN)_6\}$ acceptor unit. The consistency of the energy transfer time constants upon excitation at 400 nm and 490 nm suggests that the energy transfer occurs from the same donor state.

The broadband spectra show that upon excitation at 490 nm, the {Ru-Ru-Cr} triad **3** has ESA intensity in the blue side of the

View Article Online
DOI: 10.1039/C6CP06562G

low energy region. This is analogous to what is observed in the {Ru-Cr} complex **1** and contrasts with the {Ru-Ru} dimer **2** (no Cr), which shows transition intensity on the red side of the λ > 540 nm region. Excitation of **3** at 400 nm (Figure **S3**) likewise shows that the presence of Cr yields higher transition intensity in the same spectral region. We ascribe the late spectral profiles to a Cr-centered ^{2}MC state. The kinetic trace of dyad **1** in this region (Figure **6**, bottom panel) shows the photoinduced absorption component with a 4.1 ps rise time, indicating the population transfer into the excited state of the Cr-centered state.

The nature of the energy transfer processes. The excitation of the {Ru(tpy)(bpy)} fragment in **1** and **3** results in emission from the chromium metal center as mentioned before. The {Ru(tpy)(bpy)} fragment (donor) based emission is centered around 650-700 nm, while $\{Cr(CN)_6\}$ has a very weak transition (molar absorptivity ~0.4 $M^{-1}cm^{-1}$)[70]centered at 807 nm. These properties result on poor spectral overlap between the emission of the donor and the absorption of the acceptor and no considerable coulombic coupling between the transitions dipole moments. The possibility of wavefunction overlap leading to a Dexter mechanism can be considered as long as donor-acceptor separation is within 10 Å. For **1**, donor-acceptor distance is 5.2 Å and therefore such a model is applicable. For **3**, however the distance between the terminal Ru and Cr moiety is over 10 Å (Table **S1**). This distance may seem excessive, but one should consider the extensive through-bridge mixing between the *d* orbitals of the Ru centers suggested by the transient spectroscopy. This mixing creates a $\{Ru^{II+\delta^+}(tpy)^-(bpy)(\mu\text{-}NC)Ru^{II+\delta^+}(py)_4\}$ extended donor that can effectively engage in the energy transfer to the Cr-centered ^{2}MC state. The LUMO and HOMO of the CN bridge cannot act as traps since they are energetically higher than the populated orbitals of the ruthenium polypyridines. The insensitivity of the emission spectrum to excitation wavelength (Figure **4**) is consistent with this postulated model.

The extensive mixing between the *d* orbitals of the Ru centers observed on transient spectroscopy of the excited states can be understood taking into consideration the properties of the ligands on the coordination sphere of both Ru centers. Previous exploration of mixed-valence cyanide bridged complexes have shown that class III delocalization can be accomplished tuning the energy of the ions bound by the pseudohalide group to compensate for the intrinsic asymmetry of the cyanide bridge. For example, *trans*-$[Ru^{II}(dmap)_4\{(\mu\text{-}CN)Ru^{II}(py)_4Cl\}_2]^{2+}$ spectroscopy shows that the one electron oxidized product (**3**$^+$) is a delocalized class III mixed-valence species.[18] The spectroscopy of the one electron oxidized {Ru-Ru} dimer presented here (**2**$^{3+}$) indicates that is a localized class II mixed-valence complex (Figure **S4**). The Ru(III) is situated in the $\{Ru(py)_4\}$, as this fragment is bound to the N atom of the CN^- bridge and has a chloride anion in the coordination sphere. In the excited state of **2**$^{2+}$ the situation is very different. Now the Ru ion bound to the C atom of the bridge is ligated to a tpy anion radical, a very basic ligand, that favors formation of a Ru(III) ion in the {Ru(tpy)(bpy)} moiety and equilibrates the energy between both Ru centers, resulting in a substantial mixing of the *d* orbitals and a configuration where the unpaired electron is shared by the two ruthenium ions (Figure **9**).

The energy transfer from the Ru centers to the Cr is rather efficient. In donor-acceptor systems, the efficiency of energy transfer is calculated using $\eta = 1 - {}^{\tau_{DA}}/_{\tau_D}$, where $\tau_{D\text{-}A}$ and τ_D are the lifetimes of the donor in the presence and the absence of acceptor, respectively. For Cr based sensitization, $\tau_{D\text{-}A}$= (**1**) 4.1 ps and τ_D= 10.4 ns[‡37] hence the energy transfer efficiency is 0.99 while for the other donor-acceptor pair, $\tau_{D\text{-}A} = \tau$(**3**) = 170 ps and $\tau_D = \tau$(**2**) = 5.6 ns, with an efficiency of 0.97. The fast and efficient energy transfer exhibited by **3** makes it an attractive candidate for a molecular antennae molecule.

It is important to note that the τ = 170 ps observed for energy transfer process in **3** is more than an order of magnitude slower than the one observed for **1**. Even though, the considerable mixing between the *dπ* orbitals of the Ru ions in the $\{Ru(tpy)(bpy)(\mu\text{-}CN)Ru(py)_4\}^{3+}$ fragment allows the energy transfer to the Cr acceptor, the observed rate for energy transfer is slower as a result of a diminished overlap between the states involved, as expected when one of the components is delocalized over the two Ru units.

It is interesting to note that the long-time differential spectrum of the emissive excited state of **2** is very similar to the one observed for **3** before the energy transfer occurs. This suggests that delocalization between cyanide bridged Ru ions in the excited state could be a common occurrence when

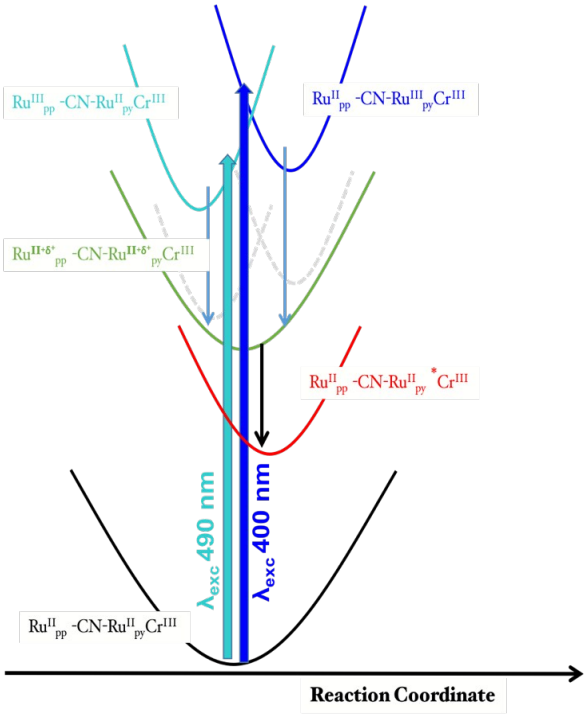

Figure 9: Cartoon representation describing the potential energy surfaces and proposed model for initial excitation with subsequent (~1.8 ps) delocalization in the excited state before the energy transfer occurs (~170 ps).

View Article Online
DOI: 10.1039/C6CP06562G

proper ligands are chosen. In fact, we venture that this kind of phenomenon might be present in some systems already reported in the literature[69, 71] where it could have been overlooked in favor of proposed cascade-type energy transfer mechanisms. In the work presented here, a detailed transient absorption analysis allowed us to experimentally corroborate how electron delocalization *in the excited state* within a multi-metallic arrangement can effectively facilitate an energy transfer process to a desired acceptor, removing the vectorial-paradigm constrain and the long distance difficulty. To the best of our knowledge, this is the first report of this phenomenon.

Conclusions

A delocalization-facilitated energy transfer process takes place in the triad compound **3**, overcoming the restrictions anticipated by a vectorial model based on independent moieties coupled through long distances. The MLCT excited states of the $\{Ru(py)_4\}$ linker are energetically the highest photoactive states in **3**. However, the role of this spacer is not only structural, but it also promotes an extensive mixing of $d\pi$ orbitals of the Ru ions in the $\{Ru(tpy)(bpy)(\mu\text{-}CN)Ru(py)_4\}$ fragment. This dual metal center moiety acts as the effective donor and leads to the efficient energy transfer process observed in **3**. This property makes this family of compounds an attractive platform for the design of antenna compounds with a broad absorption spectrum, as the properties of both fragments could be tuned independently.

.

Acknowledgements

This work was partially supported by the National Science Foundation Grant (CHE-1058638), the University of Buenos Aires (UBACyT q643 and q534), CONICET (PIP 0659) and ANPCyT (PICT 2013 0029 and PICT 2012 2041). AC acknowledges ALN for continuous support. LBV and JDH are members of the scientific staff of CONICET, and AC and PO acknowledge fellowship support from the same institution The authors gratefully thank Dr. Pablo Alborés for crystal structure refinement.

Notes and references

‡ Lifetimes: the emission lifetime of donor **1** was measured in ACN. In DMSO, we expect a shorter lifetime although this change would be negligible when evaluating such fast energy transfer rate; the reference compound is Ru(tpy)(bpy)(NCS) since the Ru is bound to the N in the NCS ligand, similarly to the bridge found in compound **3**.

REFERENCES

1. A. Harriman, M. Hissler, O. Trompette and R. Ziessel, *Journal of the American Chemical Society*, 1999, **121**, 2516-2525.
2. V. Balzani, A. Credi and M. Venturi, *Journal*, 2008, **1**, 26-58.
3. M. Furue, M. Naiki, Y. Kanematsu, T. Kushida and M. Kamachi, *Coordination Chemistry Reviews*, 1991, **111**, 221-226.
4. T. E. Knight, D. Guo, J. P. Claude and J. K. McCusker, *Inorganic Chemistry*, 2008, **47**, 7249-7261.
5. B. Xi, I. P. C. Liu, G. L. Xu, M. M. R. Choudhuri, M. C. Derosa, R. J. Crutchley and T. Ren, *Journal of the American Chemical Society*, 2011, **133**, 15094-15104.
6. M. Gagliardo, F. Rizzo, M. Lutz, A. L. Spek, G. P. M. van Klink, A. E. Merbach, L. De Cola and G. van Koten, *European Journal of Inorganic Chemistry*, 2007, **2007**, 2853-2861.
7. D. M. Guldi, *Chemical Society Reviews*, 2002, **31**, 22-36.
8. C. A. Bignozzi, R. Argazzi, J. R. Schoonover, G. J. Meyer and F. Scandola, *Solar Energy Materials and Solar Cells*, 1995, **38**, 187-198.
9. F. Puntoriero, S. Serroni, M. Galletta, A. Juris, A. Licciardello, C. Chiorboli, S. Campagna and F. Scandola, *ChemPhysChem*, 2005, **6**, 129-138.
10. K. Araki, P. Losco, F. M. Engelmann, H. Winnischofer and H. E. Toma, *Journal Of Photochemistry And Photobiology A-Chemistry*, 2001, **142**, 25-30.
11. F. Puntoriero, F. Nastasi, S. Campagna, T. Bura and R. Ziessel, *Chemistry - A European Journal*, 2010, **16**, 8832-8845.
12. M. Abrahamsson, M. Jager, R. J. Kumar, T. Osterman, P. Persson, H.-C. Becker, O. Johansson and L. Hammarstrom, *Journal of the American Chemical Society*, 2008, **130**, 15533-15542.
13. J. P. Sauvage, J. P. Collin, J. C. Chambron, S. Guillerez, C. Coudret, V. Balzani, F. Barigelletti, L. Decola and L. Flamigni, *Chemical Reviews*, 1994, **94**, 993-1019.
14. V. Balzani, A. Juris, M. Venturi, S. Campagna and S. Serroni, *Chemical reviews*, 1996, **96**, 759-834.
15. C. Chiorboli, M. T. Indelli and F. Scandola, *Topics in Current Chemistry*, 2005, **257**, 63-102.
16. A. C. Benniston and A. Harriman, *Journal*, 2008, **252**, 2528-2539.
17. P. Albores, L. D. Slep, L. S. Eberlin, Y. E. Corilo, M. N. Eberlin, G. Benitez, M. E. Vela, R. C. Salvarezza and L. M. Baraldo, *Inorganic Chemistry*, 2009, **48**, 11226-11235.
18. G. E. Pieslinger, P. Albores, L. D. Slep and L. M. Baraldo, *Angewandte Chemie - International Edition*, 2014, **53**, 1293-1296.
19. Y. Sun, Z. Chen, E. Puodziukynaite, D. M. Jenkins, J. R. Reynolds and K. S. Schanze, *Macromolecules*, 2012, **45**, 2632-2642.
20. S. J. Wu, C. Y. Chen, J. G. Chen, J. Y. Li, Y. L. Tung, K. C. Ho and C. G. Wu, *Dyes and Pigments*, 2010, **84**, 95-101.
21. C. A. Bignozzi, M. T. Indelli and F. Scandola, *Journal Of The American Chemical Society*, 1989, **111**, 5192-5198.
22. F. Scandola, R. Argazzi, C. A. Bignozzi, C. Chiorboli and M. T. Indelli, *Coord. Chem. Rev.*, 1993, **125**, 283-292.
23. R. Argazzi, C. A. Bignozzi, G. M. Hasselmann and G. J. Meyer, *Inorganic Chemistry*, 1998, **37**, 4533-4537.
24. R. Argazzi, C. A. Bignozzi, T. A. Heimer and G. J. Meyer, *Inorganic Chemistry*, 1997, **36**, 2-3.
25. K. Rangan, S. M. Arachchige, J. R. Brown and K. J. Brewer, *Energy & Environmental Science*, 2009, **2**, 410-419.

View Article Online
DOI: 10.1039/C6CP06562G

26. R. L. House, N. Y. M. Iha, R. L. Coppo, L. Alibabaei, B. D. Sherman, P. Kang, M. K. Brennaman, P. G. Hoertz and T. J. Meyer, *Journal of Photochemistry and Photobiology C-Photochemistry Reviews*, 2015, **25**, 32-45.
27. D. L. Ashford, C. R. K. Glasson, M. R. Norris, J. J. Concepcion, S. Keinan, M. K. Brennaman, J. L. Templeton and T. J. Meyer, *Inorganic Chemistry*, 2014, **53**, 5637-5646.
28. D. L. Ashford, M. K. Brennaman, R. J. Brown, S. Keinan, J. J. Concepcion, J. M. Papanikolas, J. L. Templeton and T. J. Meyer, *Inorganic Chemistry*, 2015, **54**, 460-469.
29. C. E. Welby, C. R. Rice and P. I. P. Elliott, *Angewandte Chemie-International Edition*, 2013, **52**, 10826-10829.
30. F. R. Keene, *Coordination Chemistry Reviews*, 1997, **166**, 121-159.
31. J. T. Hewitt, P. J. Vallett and N. H. Damrauer, *JOURNAL OF PHYSICAL CHEMISTRY A*, 2012, **116**, 11536-11547.
32. D. W. Thompson, A. Ito and T. J. Meyer, *Pure and Applied Chemistry*, 2013, **85**, 1257-1305.
33. J. R. Winkler, T. L. Netzel, C. Creutz and N. Sutin, *Journal of the American Chemical Society*, 1987, **109**, 2381-2392.
34. H. Hofmeier and U. S. Schubert, *Chemical Society Reviews*, 2004, **33**, 373-399.
35. D. G. Brown, N. Sanguantrakun, B. Schulze, U. S. Schubert and C. P. Berlinguette, *Journal of the American Chemical Society*, 2012, **134**, 12354-12357.
36. Q. C. Sun, S. Mosquera-Vazquez, Y. Suffren, J. Hankache, N. Amstutz, L. M. L. Daku, E. Vauthey and A. Hauser, *Coordination Chemistry Reviews*, 2015, **282**, 87-99.
37. A. Cadranel, P. Albores, S. Yamazaki, V. D. Kleiman and L. M. Baraldo, *Dalton Transactions*, 2012, **41**, 5343-5350.
38. A. Cadranel, B. M. A. Troselj, S. Yamazaki, P. Albores, V. D. Kleiman and L. M. Baraldo, *Dalton Transactions*, 2013, **42**, 16723-16732.
39. Y. Prado, L. Lisnard, D. Heurtaux, G. Rogez, A. Gloter, O. Stéphan, N. Dia, E. Rivière, L. Catala and T. Mallah, *Chemical Communications*, 2011, **47**, 1051-1053.
40. J. T. Culp, J. H. Park, F. Frye, Y. D. Huh, M. W. Meisel and D. R. Talham, *Journal*, 2005, **249**, 2642-2648.
41. B. J. Coe, T. J. Meyer and P. S. White, *Inorganic Chemistry*, 1995, **34**, 593-602.
42. P. Alborés, L. D. Slep, T. Weyhermüller, E. Rentschler and L. M. Baraldo, *Dalton transactions (Cambridge, England : 2003)*, 2006, 948-954.
43. O. D. L. O. Software package, *Journal*, 2006.
44. A. Altomare, M. C. Burla, M. Camalli, G. L. Cascarano, C. Giacovazzo, A. Guagliardi, A. G. G. Moliterni, G. Polidori and R. Spagna, *Journal Of Applied Crystallography*, 1999, **32**, 115-119.
45. G. M. Sheldrick, *Journal*, 1997.
46. G. M. Sheldrick, *Acta Crystallographica A-Foundation And Advances*, 2015, **71**, 3-8.
47. L. J. Farrugia, *JOURNAL OF APPLIED CRYSTALLOGRAPHY*, 2012, **45**, 849-854.
48. I. Noviandri, K. N. Brown, D. S. Fleming, P. T. Gulyas, P. a. Lay, A. F. Masters and L. Phillips, *The Journal of Physical Chemistry B*, 1999, **103**, 6713-6722.
49. J. P. Marcolongo, T. Weyhermuller and L. D. Slep, *Inorganica Chimica Acta*, 2015, **429**, 174-182.
50. *Journal*, 2016.
51. E. Lebon, I. M. Dixon, L. Vendier, A. Igau and P. Sutra, *Inorganica Chimica Acta*, 2007, **360**, 1235-1239.
52. I. M. Dixon, E. Lebon, G. Loustau, P. Sutra, L. Vendier, A. Igau and A. Juris, *Dalton Transactions*, 2008, 5627-5635.
53. X. J. Yang, F. Drepper, B. Wu, W. H. Sun, W. Haehnel and C. Janiak, *Dalton Transactions*, 2005, 256-267.
54. H. Nagao, T. Mizukawa and K. Tanaka, *Inorganic Chemistry*, 1994, **33**, 3415-3420.
55. P. A. Adcock, F. R. Keene, R. S. Smythe and M. R. Snow, *Inorganic Chemistry*, 1984, **23**, 2336-2343.
56. S. C. Rasmussen, S. E. Ronco, D. A. Mlsna, M. A. Billadeau, W. T. Pennington, J. W. Kolis and J. D. Petersen, *Inorganic Chemistry*, 1995, **34**, 821-829.
57. G. E. Pieslinger, P. Albores, L. D. Slep, B. J. Coe, C. J. Timpson and L. M. Baraldo, *Inorganic Chemistry*, 2013, **52**, 2906-2917.
58. C. A. Bignozzi, O. Bortolini, C. Chiorboli, M. T. Indelli, M. A. Rampi and F. Scandola, *INORGANIC CHEMISTRY*, 1992, **31**, 172-177.
59. A. V. Macatangay, S. E. Mazzetto and J. F. Endicott, *Inorganic Chemistry*, 1999, **38**, 5091-5101.
60. A. Juris, V. Balzani, F. Barigelletti, S. Campagna, P. Belser and A. Vonzelewsky, *Coordination Chemistry Reviews*, 1988, **84**, 85-277.
61. S. Campagna, F. Puntoriero, F. Nastasi, G. Bergamini and V. Balzani, ed. V. a. C. S. Balzani, Springer-Verlag Berlin, Heidelberger Platz 3, D-14197 Berlin, Germany, 2007, Vol. 280, pp. 117-214.
62. R. Siebert, C. Hunger, J. Guthmuller, F. Schlutter, A. Winter, U. S. Schubert, L. Gonzalez, B. Dietzek and J. Popp, *Journal of Physical Chemistry C*, 2011, **115**, 12677-12688.
63. M. B. Majewski, N. R. de Tacconi, F. M. MacDonnell and M. O. Wolf, *Inorganic Chemistry*, 2011, **50**, 9939-9941.
64. K. Barthelmes, M. Jager, J. Kubel, C. Friebe, A. Winter, M. Wachtler, B. Dietzek and U. S. Schubert, *Inorganic Chemistry*, 2016, **55**, 5152-5167.
65. J. D. Knoll, B. A. Albani and C. Turro, *Accounts of Chemical Research*, 2015, **48**, 2280-2287.
66. N. H. Damrauer and J. K. McCusker, *Journal Of Physical Chemistry A*, 1999, **103**, 8440-8446.
67. Q. Pan, F. Mecozzi, J. P. Korterik, J. G. Vos, W. R. Browne and A. Huijser, *ChemPhysChem*, 2016, **17**, 2654 -2659.
68. S. A. McFarland, F. S. Lee, K. Cheng, F. L. Cozens and N. P. Schepp, *Journal Of The American Chemical Society*, 2005, **127**, 7065-7070.
69. C. A. Bignozzi, R. Argazzi, J. R. Schoonover, K. C. Gordon, R. B. Dyer and F. Scandola, *Inorganic Chemistry*, 1992, **31**, 5260-5267.
70. J. J. Alexander and H. B. Gray, *Journal of the American Chemical Society*, 1968, **90**, 4260-+.
71. C. A. Bignozzi, S. Roffia, C. Chiorboli, J. Davila, M. T. Indelli and F. Scandola, *Inorganic Chemistry*, 1989, **28**, 4350-4358.